Nonlinear Dyn (2011) 66:609–623
DOI 10.1007/s11071-010-9934-9

ORIGINAL PAPER

Inelastic impact dynamics of ships with one-sided barriers. Part II: experimental validation

Ihab M. Grace · Raouf A. Ibrahim · Valery N. Pilipchuk

Received: 6 October 2010 / Accepted: 26 December 2010 / Published online: 22 January 2011

Abstract This paper is the second part of a two-part study of impact interaction of a ship roll motion with one-sided ice barrier. The first part was devoted to analytical and numerical simulations for the case of inelastic impact. The analytical approach was based on Zhuravlev and Ivanov non-smooth coordinate transformations. Extensive numerical simulations were carried out for all initial conditions covered by the ship grazing orbit for different values of excitation amplitude and frequency of external wave-induced roll moment. The basins of attraction of safe operation revealed the coexistence of different response regimes such as non-impact periodic oscillations, modulated impact motion, period added impact oscillations, chaotic impact motion and roll-over dynamics. This part presents an experimental investigation conducted on a small ship model in a tow tank. In particular, the experimental tests reveal complex dynamic response characteristics such as multi-frequency wave motion caused by the wave reflection from the tank end wall. Measured results show a good agreement with the predicted results by for small angles of the barrier relative to the ship unbiased position. However, deviation becomes significant as the angle increases. This deviation is mainly attributed to the uncertainty of the coefficient of restitution, which is found to depend on the velocity of impact in addition to the geometry and material properties of the model and barrier.

Keywords Multi-frequency waves · Coefficient of restitution uncertainty

I.M. Grace · R.A. Ibrahim (✉) · V.N. Pilipchuk
Department of Mechanical Engineering, Wayne State University, Detroit, MI 48202, USA
e-mail: Ibrahim@eng.wayne.edu

1 Introduction

The design of ships and offshore structures should take into account the effect of ice loads. In fact, ice load measurements conducted with vessels navigating in the Baltic region were found to exceed several times the design loads. The ship–ice interaction is a complex phenomenon in which interdependence exists between the ship response and ice forces. The ship response is usually influenced by transient hydrodynamics, the elastic action of the ship, large motions of the ship, the ice interaction and the presence of an ice cover. The ice failure process is, in turn, influenced by the ship response.

Most of the experimental investigations reported in the literature deal with the roll dynamics of ships in the absence of barriers. For example, comparisons of experimental measurements taken for three models (a Mariner class cargo ship, a model of the SL7 container ship, and a west coast crab fishing boat) and computational simulations of the severe roll motion and capsizing of ships operating in following seas

were presented by Fallen et al. [1]. De Kat and Pauling [2] determined the large amplitude motions of a steered vessel subjected to severe wave conditions including those that may lead to capsizing. They identified different modes of capsizing that were observed experimentally. Nayfeh [3] and Oh et al. [4] examined analytically and experimentally the loss of dynamic stability and the resulting large-amplitude roll of a vessel in a head or following sea. The existence of jump phenomena and multiple stable solutions for the case of subcritical instability was observed experimentally. The experiments also revealed that the large-amplitude roll depends on the location of the model in the standing waves. A series of capsize tests based on a prismatic ship model was conducted by Cotton and Spyrou [5] with the purpose of studying the significance of some nonlinear phenomena predicted by theoretical studies of roll motion. In particular, regions of bi-stability were observed near linear resonance. It was verified that, near resonance, the frequency-response curve is skewed towards lower frequencies due to the softening nature of the righting arm curve. The measured capsize boundary is then compared with the theoretical one. Some sensitivity of capsize to initial conditions was discussed and applied to experimental tests.

The results of free oscillation tests on an unappended prismatic hull with 30 degrees of deadrise were reported by Brown and Klosinski [6]. The roll period and logarithmic decrement were determined from test records. The added mass moment of inertia and damping in roll were deduced from measured data based on the linear damped harmonic oscillator. Empirical expressions for the inertia and damping were presented and compared with the measured results. These expressions were used to predict the rolling characteristics of a prototype 100 ft. boat. Atsavaprance et al. [7] conducted a series of model tests to explore the mechanisms of roll damping around a conventional combatant hull form (DTMB model #5617) and an advanced tumble-home hull form (DTMB model #5613-1). Both free roll decay and forced oscillation experiments were carried out in calm water and in waves over some range of forward speeds. The experimental results were utilized to develop empirical and analytical roll damping models and to validate the accuracy of simulation programs in the calculation of various components of hydrodynamic forces. The viscous drag coefficients were found to strongly depend on ship forward speed and roll amplitude, but the added mass coefficients were found relatively constant for the considered range of forward speed and roll amplitude. Other experimental validations of ship roll damping were also reported in [8, 9].

Bullian and Francescotti [10] conducted a series of experimental tests in regular beam waves on a trimaran and a pentamaran to study the effect of transversal hull separation on roll motion in waves. Four different configurations for the trimaran were tested in beam waves and two for the pentamaran using the same main hull. The experiments in regular waves revealed the extreme sensitivity of these hull typologies to roll motion in beam waves, even under mild sea waves (wave steepness $= 1/60$). Two configurations of the trimaran and one of the pentamaran exhibited a multi-valued roll response curve in the low frequency range. Other observations confirmed that multi-hulls can be characterized by large rolling motions and the presence of bifurcations and jumps of amplitude when the outriggers are 'narrow and shallow'. The trimaran configuration with mild wave steepness was found to exhibit the same roll amplitude as a monohull having the same length at waterline. Other configurations exhibited smaller roll amplitudes, but were in any case more than twice those tested in [11–13]. It was found that the rolling behavior of pentamaran configurations has a strongly nonlinear feature compared with that of trimarans with similar spacing. The reason was attributed to the different tested GM (the distance between the ship center of mass, G, and its metacenter, M) values.

As mentioned earlier, this part is devoted to experimental investigations of impact interaction of ships with one sided barrier placed at different values of impact roll angle. Section 2 presents the model and experimental set-up used in the present study. The experimental results under two wave maker speeds are then discussed in terms of time and frequency domains together with phase portraits. The experiments are conducted for different values of barrier position. In order to compare the measured results with those predicted in Part I, Sect. 2.3 describes the model parameter identification that can be used in the analytical model and a comparison with analytical results. It is found that the measured coefficient of restitution experiences uncertainty due to uncertainties in the impact relative velocity.

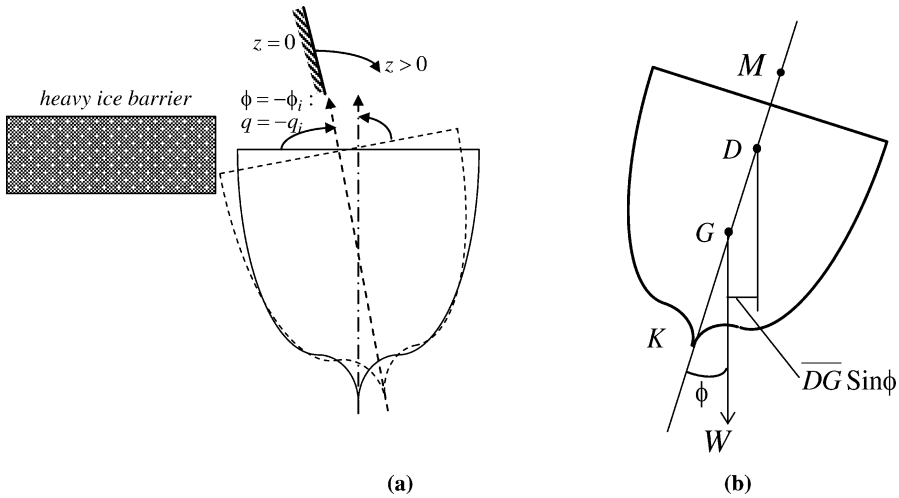

Fig. 1 Schematic diagram of ship in roll motion showing (**a**) one-sided ice barrier impact and (**b**) the location of the model center of mass G, metacenter, M, and suspension point, D

2 Experimental investigation

2.1 The model and experimental set-up

A wooden ship model of a relatively small scale is selected to satisfy two-dimensional wave condition. The ship model's metacentric height, mass moment of inertia, and center of gravity are determined experimentally. The metacentric height of a ship is defined as the distance from the metacenter to the center of gravity and obtained by means of the same procedure outlined in Bhattacharyya [14]. With reference to Fig. 1(b), the following parameters of the model are obtained: height of the metacenter $\overline{GM} = 7.7$ mm, weight of the model $W = 8.6$ N, mass moment of inertia about the longitudinal axis $J_G = 0.00237$ Kg m^2, $\omega_n = 4.83$ rad/s, and $\overline{KG} = 60$ mm.

Figure 2 shows a block-diagram of the test setup. The towing tank is a rectangular Plexiglas with outside dimensions $3.05 \times 1.22 \times 1.22$ m and thickness 0.03175 m. The tank is mounted on a steel frame with six adjustable legs. The frame is designed such that the length of each leg can be adjusted separately in order to keep the tank in a horizontal level regardless of the floor irregularities. The ship model is only allowed to roll about the longitudinal axis that passes through its center of gravity against one-sided barrier as shown in Fig. 3. An axle is fitted inside the model along the longitudinal axis, which is linked with a metallic beam that is fixed to the carrying carriage. For other purposes, the carrying carriage is allowed to move forward and backwards in a straight line parallel to longitudinal axis of the tank through a DC gear motor.

The towing tank is equipped with a flap-type wave maker capable to generate water waves at different wave heights and wavelengths. The speed of the gear motor is controlled by a speed control unit such that the motor speed can be adjusted up to 34 rpm. The tests are conducted at a speed very close to the resonant frequency of the water free surface. Neglecting the surface tension, the natural frequency of the free surface in a rectangular tank is estimated from the formula [15]

$$\omega_m^2 = \frac{2m\pi}{L} g \tanh\left(\frac{2m\pi}{L} H\right), \quad m = 1, 2, \ldots, \qquad (1)$$

where L is the inside length of the tank, and $H = 0.89$ m is the water depth; according to (1), the first natural frequency of the free surface is $\omega_1 = 4.4$ rad/s.

The wave height of the water free surface is measured by a resistance wave gauge consisting of two electrical wires (material C72150, 0.287 mm diameter, and resistance 7.62 ohms/m) uniformly spaced at a separating distance of 4 mm. The zero water level was identified by running the data acquisition tool under no wave conditions. The pair of wires is stretched between the tank bottom and its top and attached to the inside wall of the tank. The amplitude of the model roll angle is measured using an analog magnetic angle sensor (ASM GmbH Automation PRAS2) with a range from $-90°$ to $90°$.

2.2 Experimental results

In order to determine the effect of the barrier position on the ship response, each set of tests is carried out at

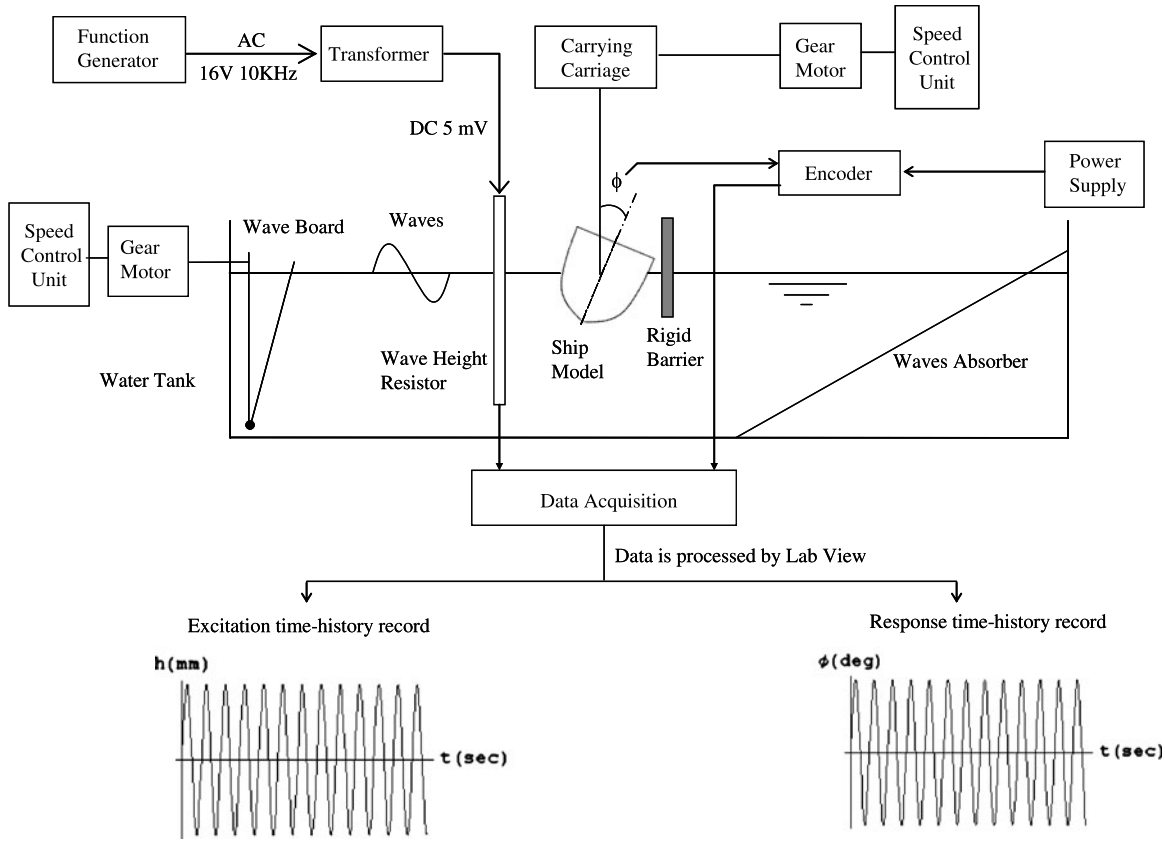

Fig. 2 Block diagram showing the experiment layout

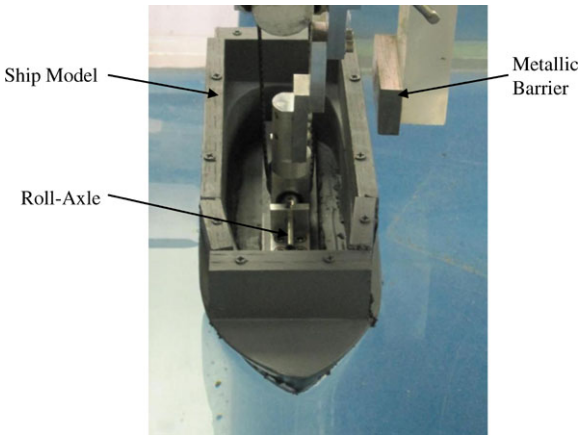

Fig. 3 The ship model showing the installed axle about which the model is restricted to roll against one-sided barrier shown on its right side

the same motor speed at different values of initial impact angle. The first set of tests is carried out at a motor speed $N_m = 2.4$ rad/s. Figures 4(a) and 4(b) show the time history record and magnification of few cycles, revealing the longer time duration of the wave elevation than deepening. The areas under the positive and negative portions of the diagram are equal, giving zero average mean of the wave profile. This is reflected in the FFT of the time history record as given in Fig. 4(c). It is seen that the free surface wave height is periodic with two major frequencies, which may be attributed to the wave reflection from the opposite wall of the tank. The roll angle response of the model experiences amplitude modulation such that the roll angle varies between $-54°$ and $58°$ as shown in Fig. 5(a). Figures 4(c) and 6(a) show FFT plots of liquid surface elevation and the roll angle response, respectively. The nonzero mean amplitude is revealed on the FFT plots at zero frequency. Moreover, it can be seen that the ship response exhibits amplitude modulated cycles whose frequency content complies with those of the liquid surface elevation; see also the amplitude–velocity diagram in Fig. 7(a). The first frequency is

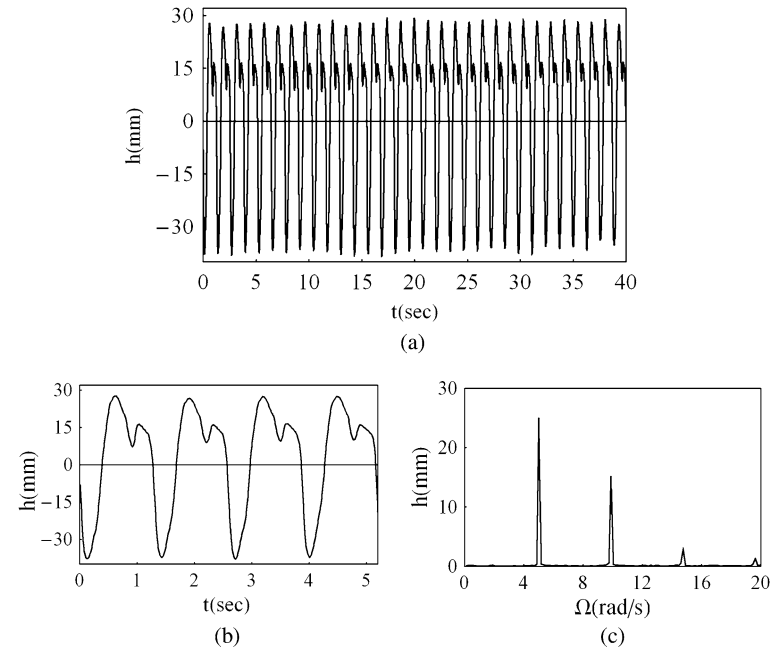

Fig. 4 Free surface wave at wave maker motor speed $N_m = 2.4$ rad/s: (**a**) time history record of the water free surface, (**b**) magnification of few cycles showing the duration of positive and negative wave profile, (**c**) FFT plot

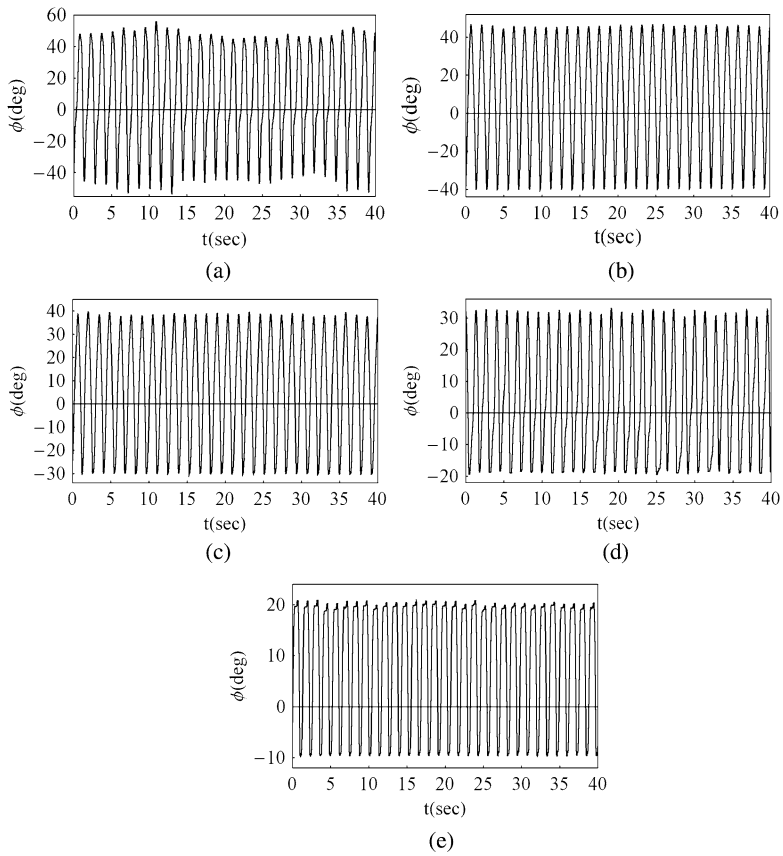

Fig. 5 Measured time history records of the model response under motor speed $N_m = 2.4$ rad/s: (**a**) in the absence of barrier, (**b**) in the presence of one-sided barrier at $-40°$, (**c**) at $-30°$, (**d**) at $-20°$, (**e**) at $-10°$

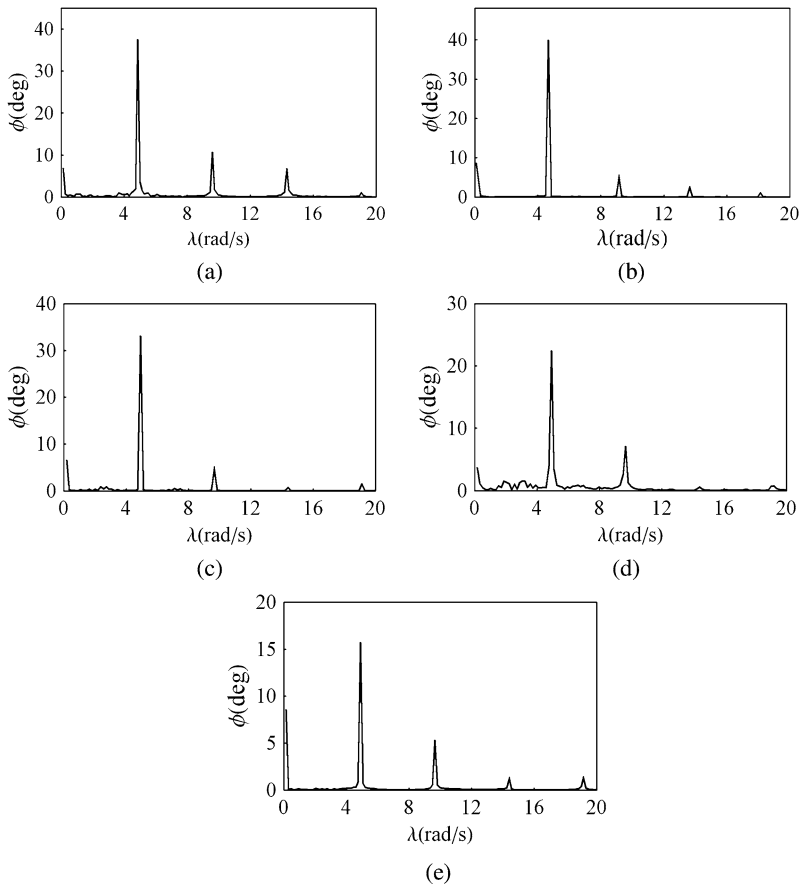

Fig. 6 FFT plots of the time history records of the model response of Fig. 5 under motor speed $N_m = 2.4$ rad/s: (**a**) in the absence of barrier, (**b**) in the presence of one-sided barrier at $-40°$, (**c**) at $-30°$, (**d**) at $-20°$, (**e**) at $-10°$

4.8 rad/s, which is twice the motor speed. This is due to the fact that for every motor's cycle, there are two effective strokes by the wave maker board: one in the forward direction, and the other in the backward direction. The response of the ship model is almost periodic with a principle frequency of 4.8 rad/s as shown in Fig. 6(a). This is confirmed by the phase plot shown in Fig. 7(a).

By placing a rigid barrier in the vicinity of the model at four different orientations, $\phi_i = -40°$, $-30°$, $-20°$ and $-10°$ for the same motor speed, $N_m = 2.4$ rad/s, the time history records for the ship roll angle response are shown in Figs. 5(b)–5(e). It is seen that the ship experiences a single impact every excitation period. With reference to Fig. 5(b), the maximum roll angle amplitude in the positive direction is 46° which is greater than the magnitude of the impact angle $\phi_i = -40°$, and yet smaller than the maximum positive angle in the absence of the barrier. This effect may be contributed to the energy loss at the barrier and phase shift variations induced by interactions with the barrier. The corresponding FFT plots and phase plots of the model response are shown in Figs. 6(b)–6(e) and 7(b)–7(e), respectively. In particular, Fig. 7(b) shows the 'phase plot' of the model response for impact angle $\phi_i = -40°$, at which the velocity jump occurs. It should be noted that a small velocity jump that occurs at $\phi = 46°$ is possibly due to the stick–slip phenomenon between the ship model and the shaft about which the model rolls. As a result, a new feature appears in the time history record for the case of impact angle $\phi_i = -10°$. It can be seen that the maximum roll amplitude is close to 22°. Also, the model response shown in Fig. 5(e) exhibits flattening at the positive peak at an angle less than 20°. By looking at the signal of the water free surface waves at this instant of time, one may conclude that the forward wave and the reflected wave are having opposing effect and keep the position of the model for a duration less than 0.5 s. This is reflected in the corresponding phase diagram by the near zero velocity near $\phi \approx 20°$ as shown in Fig. 7(e).

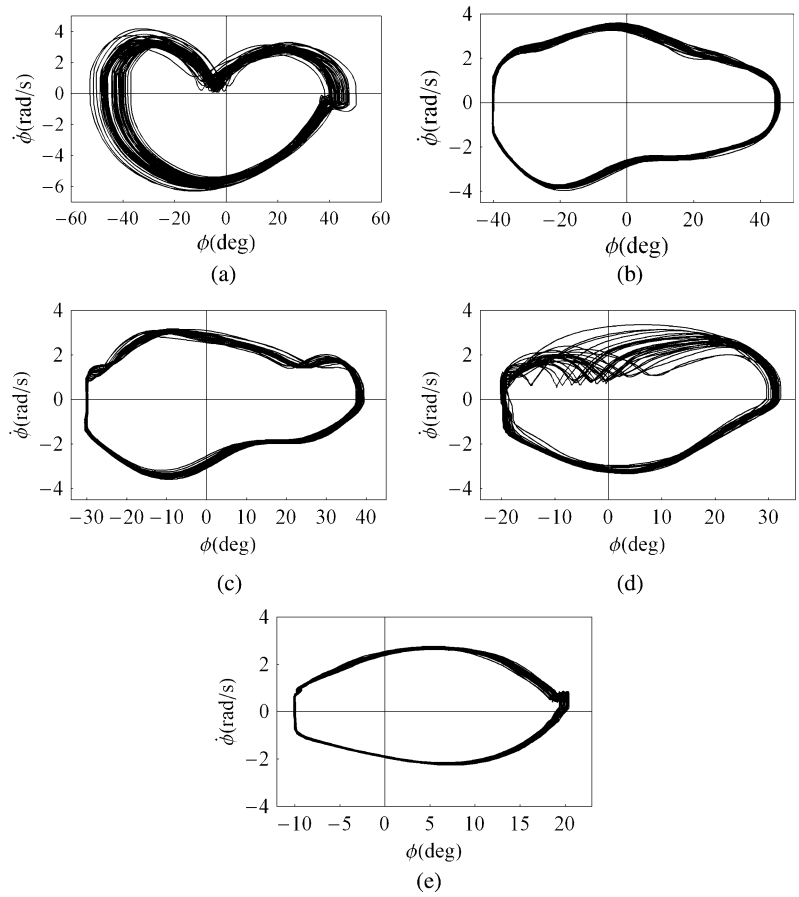

Fig. 7 Phase portraits of the time history records of the model response of Fig. 5 under motor speed $N_m = 2.4$ rad/s: (**a**) in the absence of barrier, (**b**) in the presence of one-sided barrier at $-40°$, (**c**) at $-30°$, (**d**) at $-20°$, (**e**) at $-10°$

Another set of experiments is conducted at a motor speed of $N_m = 2.8$ rad/s. This frequency is close to the resonance of the water free surface, leading to large wave heights with the possibility of nonlinear effects. Figures 8, 9(a), 10(a), and 11(a) show profiles of the water free surface wave and the model response in the absence of a barrier. In particular, it can be seen from Fig. 8 that for this case, the wave generates a multiple frequency excitation of the ship model with the possibility of nonlinear effects. The FFT plots of the water free surface wave and model response are displayed in Figs. 8(b) and 10(a), respectively. The principal frequency of waves is 5.6 rad/s, which is twice the motor speed. Also, the model response is modulated with two frequencies within the range from $-60°$ to $57°$. The response of the ship model is close to periodic as shown in Fig. 11(a).

For the barrier placed at four different positions, $\phi_i = -40°, -30°, -20°$ and $-10°$, and under the same motor speed, $N_m = 2.8$ rad/s, the time history records for the ship roll angle response are shown in Figs. 9(b)–9(e). These plots reveal that the impact interaction with the barrier may occur in a regular or irregular way and with different cycle rate as the barrier position is changed. Furthermore, as the impact angle is reduced towards $\phi_i = -10°$, the model experiences multi-frequency oscillations as reflected in the FFT plots and phase portraits shown in Figs. 10 and 11, respectively. (It should be noted that other experimental tests, not reported in this paper, revealed new phenomena such as sticking and chattering motion at relatively smaller impact angles.)

The Fourier spectra presented in Fig. 10 may not reveal possible non-stationary effects in the frequency response caused by impact events. This can be obtained either by using the windowed Fourier transform or the wavelet transform. The present work adopts wavelet transform because the windowed Fourier transform relies on the selected length of the window. Thus, any special features occur during short timescales smaller than the length of the window, or with small frequencies than those contained in the win-

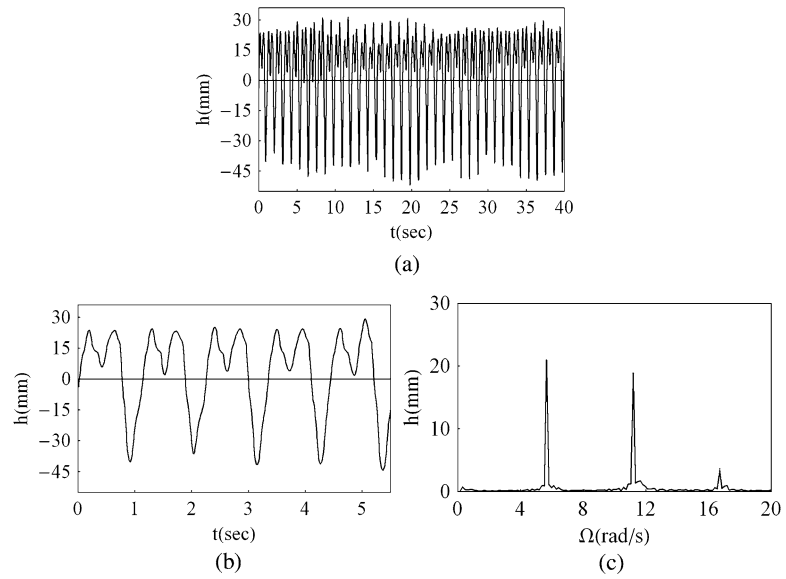

Fig. 8 Free surface wave at wave maker motor speed $N_m = 2.8$ rad/s: (**a**) time history record of the water free surface, (**b**) magnification of few cycles showing the duration of positive and negative wave profile, (**c**) FFT plot

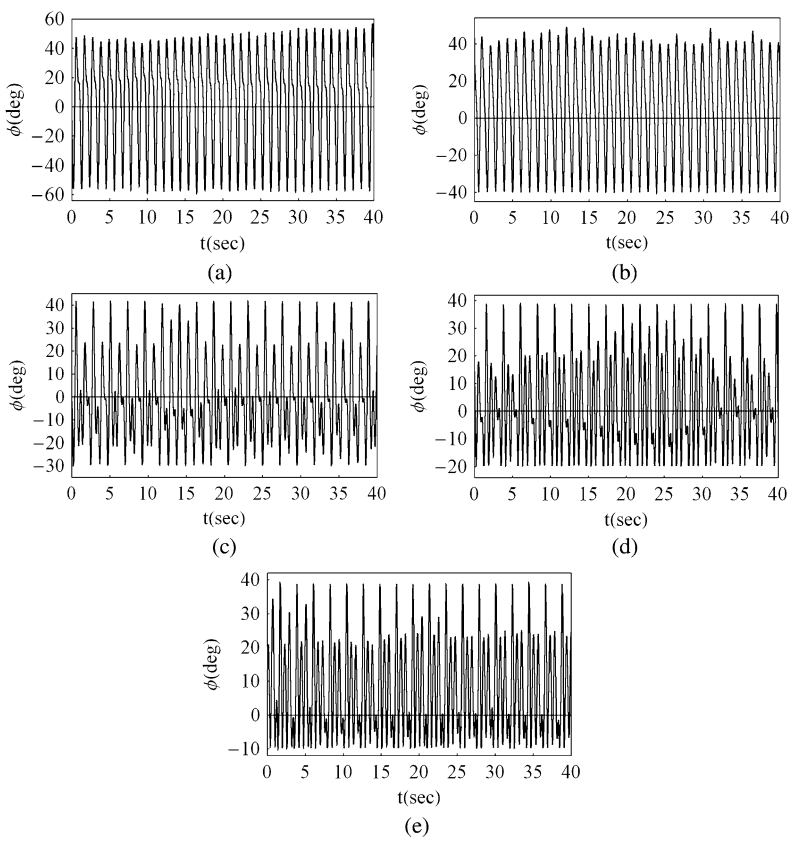

Fig. 9 Measured time history records of the model response under motor speed $N_m = 2.8$ rad/s: (**a**) in the absence of barrier, (**b**) in the presence of one-sided barrier at $-40°$, (**c**) at $-30°$, (**d**) at $-20°$, (**e**) at $-10°$

dow are lost and cannot be captured by the windowed Fourier transform. On the other hand, the wavelet transform has the advantage in that it follows the rapid variations of the instantaneous frequencies since it adjusts the length of the window according to the frequency content of the signal.

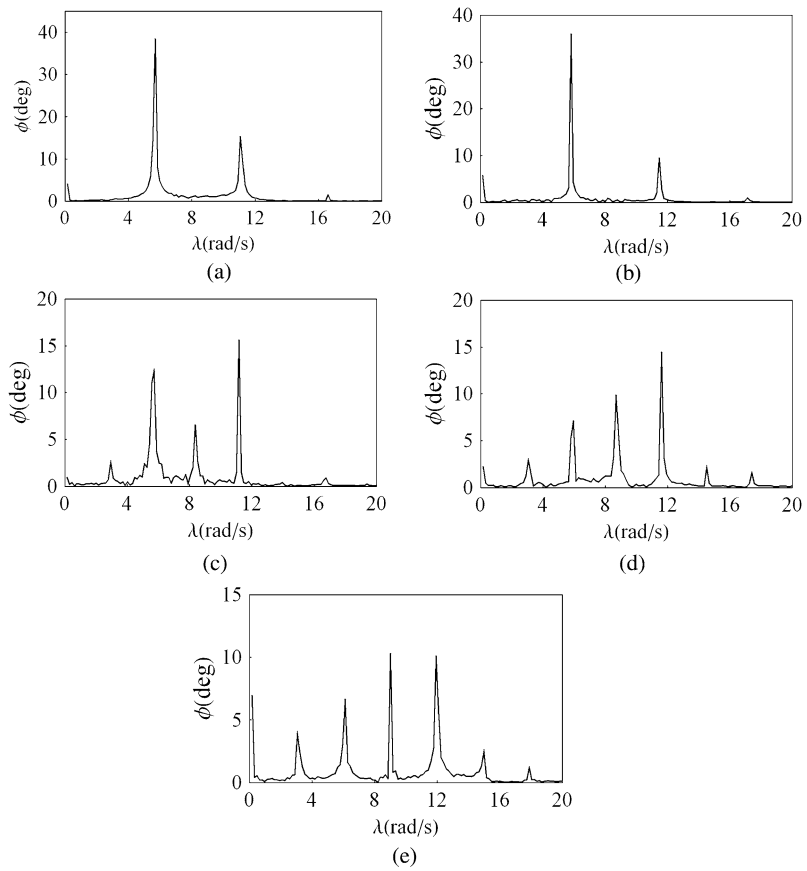

Fig. 10 FFT plots of the time history records of the model response shown in Fig. 9 under motor speed $N_m = 2.8$ rad/s: (**a**) in the absence of barrier, (**b**) in the presence of one-sided barrier at $-40°$, (**c**) at $-30°$, (**d**) at $-20°$, (**e**) at $-10°$

Figure 12 shows Morlet wavelet plots of the model response shown in Fig. 9 under a motor speed $N_m = 2.8$ rad/s. A brief account of wavelet transform and Morlet wavelet is given in the Appendix. The plots shown in Fig. 12 are generated using the MATLAB command: ccfs = cwt(x, 1:128, 'morl', 'lvlabs'); where x is the input signal. While the wavelet scale content is quite stationary in the fragments of Figs. 12(a) and 12(b), related to larger impact angles, observable non-stationary effects occur when the barrier is shifted towards the ship's port side; see fragments of Figs. 12(c) through 12(e). Although, at the very small impact angle, see Fig. 12(e), the non-stationary features are less clear. Since the motor speed is fixed, such non-stationary effects may be due to redistribution in the component amplitudes rather than varying frequencies. Figure 12(f) provides the linear dependence of the computed pseudo-period on the scale (dilation).

2.3 Identification of model parameters and modeling the coefficient of restitution

The main purpose of this section is to compare the analytical results with experimental measurements in order to establish the validity of the analytical approaches reported in Part I of the present study. The nonlinear equation of the ship roll dynamics given by (2) in Part I needs to be modified, however, to account for the possible influence of dry friction damping between the ship model and the shaft about which the model rolls, in addition to the encoder resistance. Since the friction force acts in the opposite direction to the velocity, as well as the encoder resistance, one may define a total effective dry friction moment M_f of constant amplitude and in the opposite direction to the velocity, $M_f\,\mathrm{sgn}(\dot{\phi})$, where M_f can be identified experimentally. In this case, the equation of motion takes the form

$$\ddot{\phi} + 2\zeta\omega_n\dot{\phi} + M_f\,\mathrm{sgn}(\dot{\phi}) + a\dot{\phi}|\dot{\phi}| + \omega_n^2\phi + c_3\phi^3 + c_5\phi^5 = \xi(t). \quad (2)$$

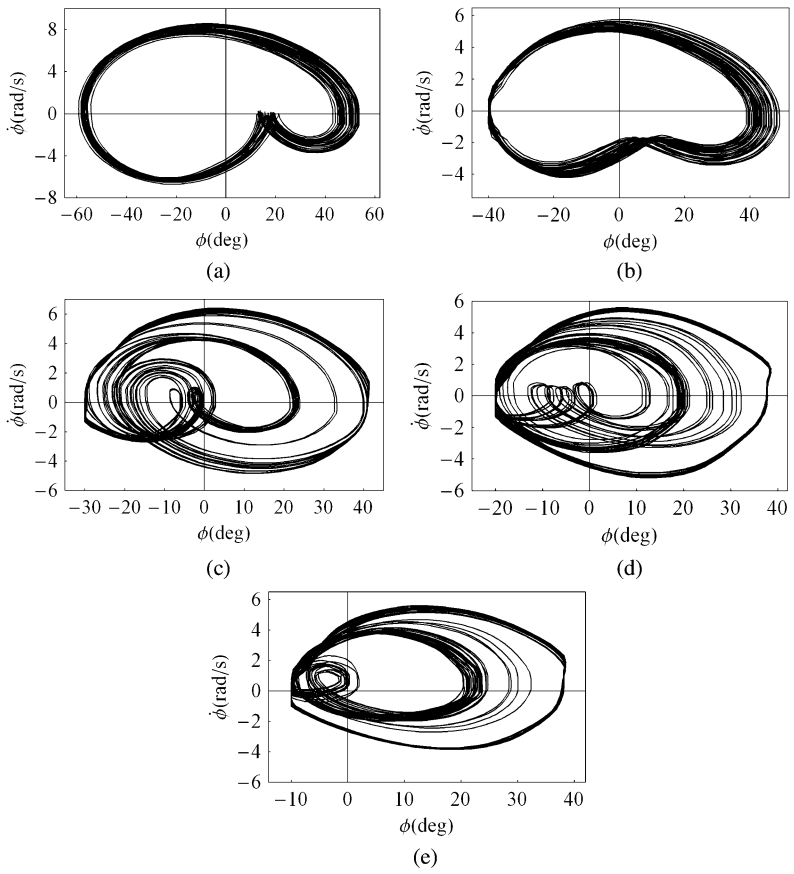

Fig. 11 Phase portraits of the time history records of the model response shown in Fig. 9 under motor speed $N_m = 2.8$ rad/s: (**a**) in the absence of barrier, (**b**) in the presence of one-sided barrier at $-40°$, (**c**) at $-30°$, (**d**) at $-20°$, (**e**) at $-10°$

The excitation moment $\xi(t)$ can be represented as follows [16, 17]:

$$\xi(t) = \alpha_0 \omega_n^2 \pi \sum_{i=1}^{N} \frac{h_i}{\lambda_i} \cos(\Omega_i t + \varepsilon_i), \tag{3}$$

where α_0 is the effective wave slope coefficient, h_i is the ith wave amplitude component, and ε_i is the corresponding phase angle, and λ_i is the wavelength given by the expression

$$\lambda_i = \frac{2\pi g}{\Omega_i^2}. \tag{4}$$

Substituting (4) into (3) gives

$$\xi(t) = \frac{\alpha_0}{2g} \omega_n^2 \sum_{i=1}^{N} h_i \Omega_i^2 \cos(\Omega_i t + \varepsilon_i). \tag{5}$$

Adopting Ivanov transformation (model 2 of Part I),

$$\begin{aligned} &\phi = S\,\mathrm{sgn}(S) - \phi_i \quad \text{and} \\ &\dot{\phi} = \mathrm{sgn}(S)\big[1 - K\,\mathrm{sgn}(SV)\big]V, \end{aligned} \tag{6}$$

brings (2) to the form of the dynamical system

$$\begin{aligned} \dot{S} &= \big[1 - K\,\mathrm{sgn}(SV)\big]V, \\ \dot{V} &= -2\zeta\omega_n V - aV\big|\big[1 - K\,\mathrm{sgn}(SV)\big]V\big| + \mathrm{sgn}(S) \\ &\quad \times \left[\frac{1 + K\,\mathrm{sgn}(SV)}{1 - K^2}\right] \\ &\quad \times \big\{-\omega_n^2\big(S\,\mathrm{sgn}(S) + \phi_i\big) - c_3\big(S\,\mathrm{sgn}(S) + \phi_i\big)^3 \\ &\quad - c_5\big(S\,\mathrm{sgn}(S) + \phi_i\big)^5 - M_f\,\mathrm{sgn}(\dot{\phi}) + \xi(t)\big\} \end{aligned} \tag{7}$$

where S and V are the new coordinates whose values are not restricted, $K = (1 - e)/(1 + e)$, and e is the coefficient of restitution.

The identification of the model parameters is carried out by conducting a free vibration test. In particular, the natural frequency of the ship model is found

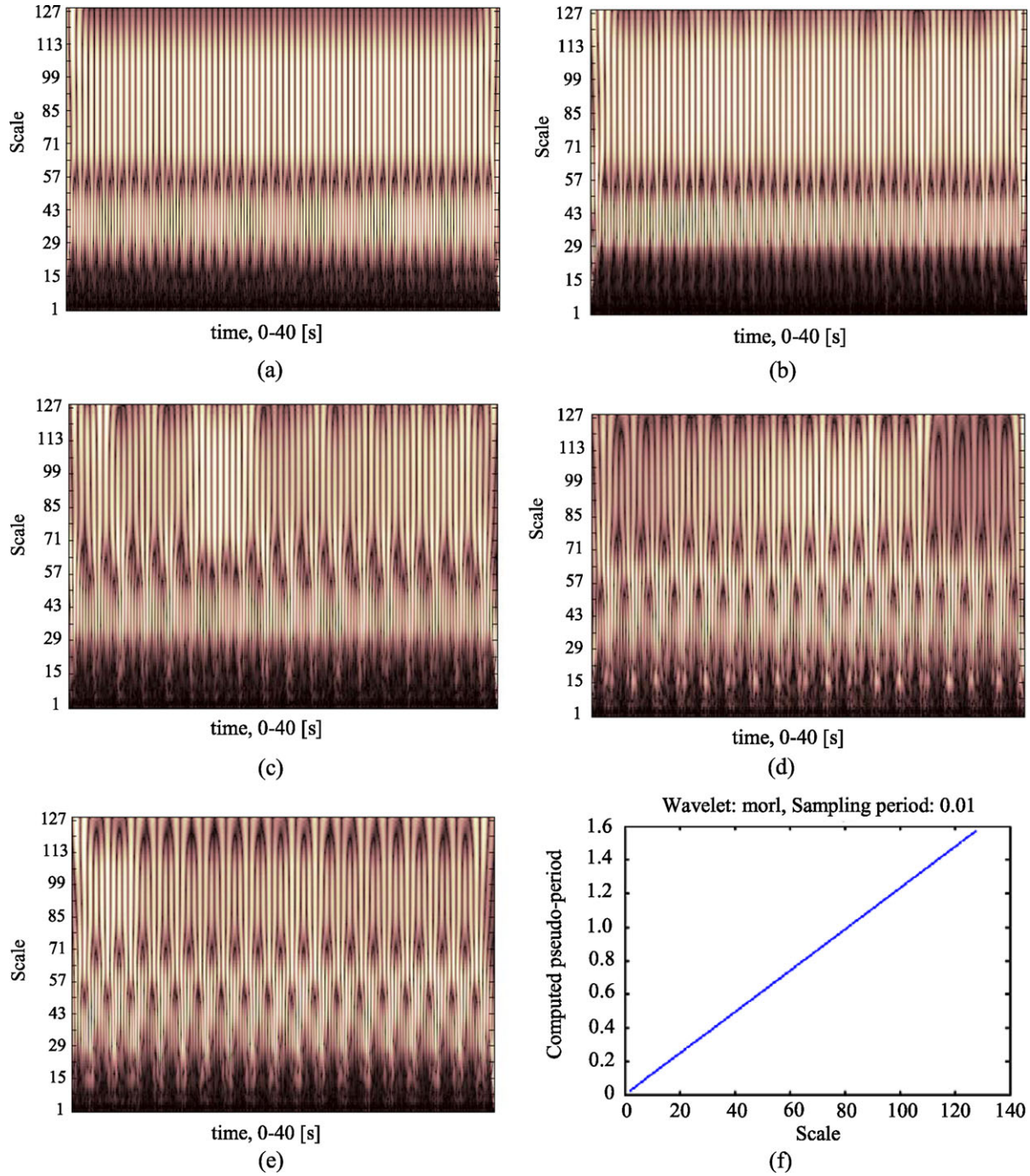

Fig. 12 Morlet wavelet plots of the model response shown in Fig. 9 under motor speed $N_m = 2.8$ rad/s: (**a**) in the absence of barrier, (**b**) in the presence of one-sided barrier at $-40°$, (**c**) at $-30°$, (**d**) at $-20°$, (**e**) at $-10°$, and (**f**) shows the quasi period versus scale relationship

to be $\omega_n = 4.2$ rad/s while the linear damping factor is $\zeta = 0.14$. Recall that the restoring moment is given by

$$\Gamma(\phi) = \omega_n^2 \phi + C_3 \phi^3 + C_5 \phi^5. \tag{8}$$

The restoring moment vanishes (i.e., $\Gamma(\phi) = 0$) at the ship model capsizing angle which is measured and its value is found to be $\phi_c = 82°$. Also, the restor-

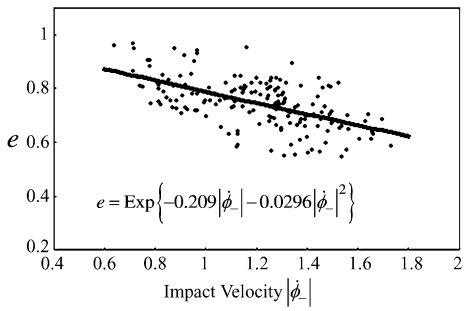

Fig. 13 Dependence of the coefficient of restitution on the impact velocity (the fitting curve is exponential: $e = \mathrm{Exp}\{-0.209|\dot{\phi}_-| - 0.0296|\dot{\phi}_-|^2\}$)

ing moment vanishes at the inverted position of the ship, $\phi = 180°$. This gives two algebraic equations whose solution is found to be $C_3 = -10.42$ 1/s^2 and $C_5 = 0.87$ 1/s^2.

The coefficient of restitution is measured from impact tests described in the previous subsection using the basic definition $e = |\dot{\phi}_+/\dot{\phi}_-|$, where $\dot{\phi}_+$ and $\dot{\phi}_-$ are the ship model velocities just after and before impact, respectively. In most engineering applications, the coefficient of restitution has been assumed to be a constant that depends on the geometry and properties of colliding bodies. However, in the present experimental investigation it is found that the coefficient of restitution e depends also on the velocity just before impact and its value is unrepeatable in every cycle and in every test. Some studies in other applications confirmed this observation. For example, in impact analysis of multibody dynamics considered by Schiehlen and Seifried [18], the multiple impacts in every test were found to be the source of the uncertainty of the coefficient of restitution and depend on the velocity. It was shown that for the case of rod impacts, the coefficient of restitution decreases monotonically with increasing initial velocity. Note that the coefficient of restitution depends also on the angle of tilting of the model during the impact and dry friction due to oblique impact against a barrier.

Ronsse and Sepulchre [19] showed that the acceleration of the table with a bouncing ball at impact is an important parameter for the robustness of the feedback system to model uncertainty, in particular to the uncertainty on the coefficient of restitution. Figure 13 shows the dependence of the coefficient of restitution on the velocity of the model just before impact. It is seen that the dependence is scatter. The curve fitting of the measured points reveal a monotonic decrease with the impact velocity. The curve fitting is based on selecting the exponential form:

$$e = \mathrm{Exp}\left\{\varsigma_1|\dot{\phi}_-| + \varsigma_2|\dot{\phi}_-|^2\right\}, \tag{9}$$

where ς_1 and ς_2 are chosen to satisfy the boundary conditions $e = 1$ at $|\dot{\phi}_-| = 0$, and $e = 0$ at $|\dot{\phi}_-| = \infty$.

The reason for selecting expression (9) is that it provides a natural and smooth transition between the two asymptotic limits. For motor speed $N_m = 2.4$ rad/s, the average value of the coefficient of restitution estimated from the time history records shown in Figs. 5(b)–5(e) is found to be $e = 0.73$. This value is adopted for the numerical simulation.

In order to determine the nonlinear damping coefficient a and the effective friction parameter M_f, the test results given in Figs. 4, 5(a) and 6(a) were used. System (2) is solved numerically for different values of a and M_f, and the value of a and M_f are chosen to minimize the error in response as compared to the experimental result given in Fig. 14(a). Such a parameter optimization procedure gives $a = 0.05$ and $M_f = 0.84$ 1/s^2.

Equations (7) are solved numerically to predict the model response. Figure 14 shows the time history records of the steady state response measured experimentally and those predicted numerically for different barrier positions. Figure 15 shows the corresponding FFT plots. Figure 15 shows the FFT plots related to Fig. 14, and both plots reveal multiperiodic response with the same frequency components. However, it is seen that the predicted amplitude in both time history record and FFT plot is larger than the measured one. Such deviation may be attributed to the uncertainty in the coefficient of restitution.

3 Conclusions

Early experimental tests revealed new phenomena not predicted by the numerical simulation such as sticking and chattering motion at relatively smaller impact angles. Some other discrepancies between the measured results and those predicted by numerical simulation are mainly attributed to the reflective waves from the end wall of the towing tank. This causes the well known hydrodynamic memory effect. In order to have

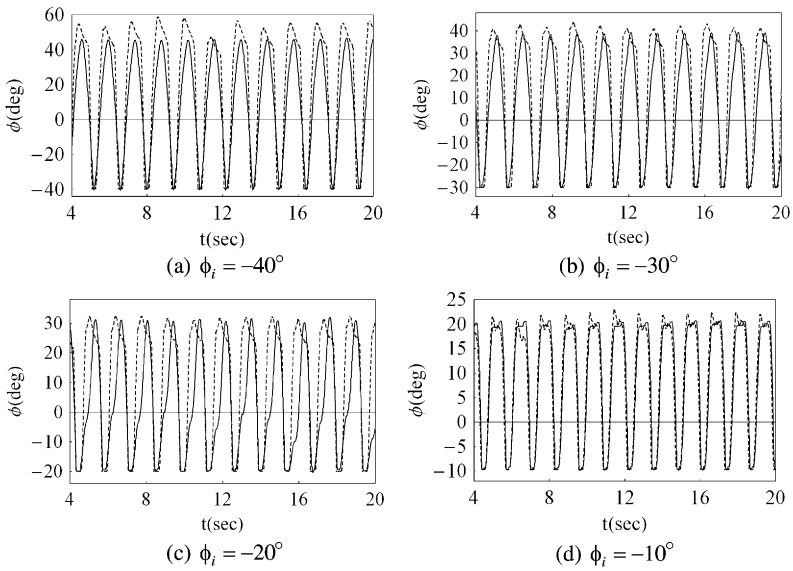

Fig. 14 Comparison between measured and predicted time-history record of ship response for $N_m = 2.4$ rad/s and different impact angles, —— experimental measurement, - - - - numerical simulation

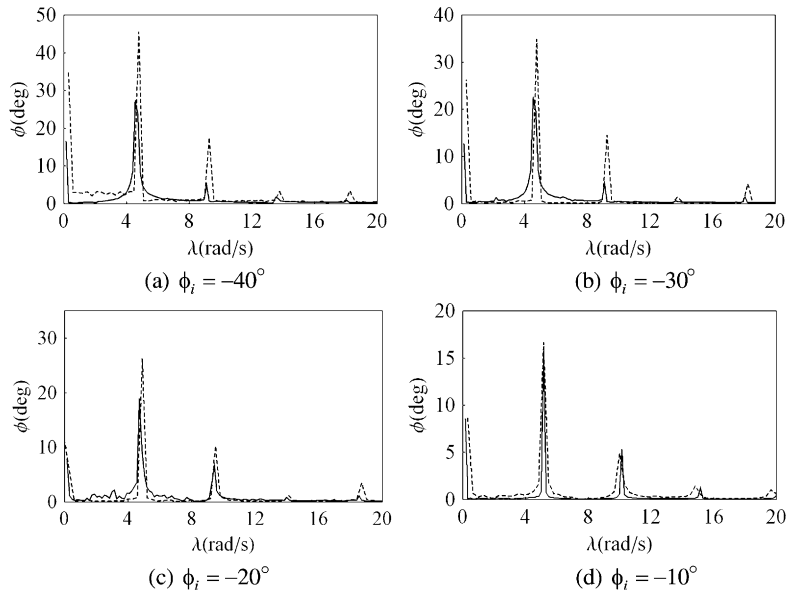

Fig. 15 Comparison between measured and predicted results FFT of ship time history responses shown in Fig. 13 for $N_m = 2.4$ rad/s and different values of impact angle. —— experimental measurement, - - - - numerical simulation

an accurate comparison with the test results, the excitation to the ship roll motion must be modified to include two frequency sine waves with proper phase angle that matches the measured wave. Furthermore, the reflected waves were minimized by placing a perforated board at the tank end at an angle 25° with the tank floor. The model was modified to take into account the friction between the model axle of rotation and its bearing as well the friction in the angular encoder, and also the actual wave components. The measured coefficient of restitution in every test was found to exhibit uncertainty and dependency of the impact velocity. This, of course, contributed to deviation between the predicted and measured results. The magnitude of deviation was found to diminish as the impact angle approaches $\phi_i = -10^\circ$. The uncertainty and quantification of uncertainty in the coefficient of restitution and its influence on the model behavior is the subject of independent study.

Acknowledgement This research is supported by a grant from ONR under Award No.: N00014-05-1-0040. Dr. Kelly B. Cooper is the Program Director.

Appendix: Wavelet transform

The wavelet transform of a continuous time signal, $x(t)$, is obtained by using discrete values of the dilation (or scale) s, and time translation u of the wavelet function $\psi_{u,s}(t)$. The wavelet transform of a continuous signal, $x(t)$, using discrete wavelets is

$$T_{u,s}x(u,s) = \int_{-\infty}^{\infty} x(t)\psi_{u,s}(t)\,dt, \tag{A.1}$$

where $\psi_{u,s}(t)$ is a wavelet function for which the family

$$\psi_{u,s}(t) = \frac{1}{\sqrt{s}}\psi\left(\frac{t-u}{s}\right) \tag{A.2}$$

forms an orthonormal basis. By choosing an orthonormal wavelet basis, $\psi_{u,s}$, one can reconstruct the original signal in terms of wavelet coefficients, $T_{u,s}$, using the inverse discrete wavelet transform as follows

$$x(t) = \sum_{s=-\infty}^{+\infty}\sum_{u=-\infty}^{+\infty} T_{u,s}\psi_{u,s}(t). \tag{A.3}$$

Orthonormal dyadic discrete wavelets are associated with scaling functions, $\phi_{u,s}(t)$, which have the same form as the wavelet functions described by (A.2)

$$\phi_{u,s}(t) = \frac{1}{\sqrt{s}}\phi_{u,s}\left(\frac{t-u}{s}\right). \tag{A.4}$$

A continuous approximation signal $x(t)$ at scale index s can be generated as a sum of a sequence of scaling functions at the scaling factor by the approximation coefficients as follows [20]:

$$x_s(t) = \sum_{u=-\infty}^{\infty} S_{u,s}\phi_{u,s}(t) \to x(t) \quad \text{as } s \to -\infty, \tag{A.5}$$

where $S_{u,s}$ are the *approximation coefficients* and $x_s(t)$ is a smooth scaling-function-dependent version of the original signal $x(t)$ at scale index s. The scaling functions can be convoluted with the signal to produce the approximation coefficients

$$S_{u,s} = \int_{-\infty}^{\infty} x(t)\phi_{u,s}(t)\,dt. \tag{A.6}$$

The continuous approximation given by (A.5) approaches $x(t)$ at small scales, i.e., as $s \to -\infty$. In the present work, the *Morlet wavelet,* is adopted and is defined by the expression [20]

$$\psi(t) = \pi^{-1/4}\left[e^{i2\pi f_0 t} - e^{-(2\pi f_0)^2/2}\right]e^{-t^2/2}, \tag{A.7}$$

where f_0 is the central frequency of the mother wavelet. The second term in the brackets is known as the correction term, as it corrects for the non-zero mean of the complex sinusoid of the first term. In practice, it becomes negligible for large enough f_0 and can be ignored, in which case, the Morlet wavelet can be written in a simpler form as

$$\psi(t) = \frac{1}{\pi^{1/4}}e^{i2\pi f_0 t}e^{-t^2/2}. \tag{A.8}$$

The Morlet wavelet is simply a complex wave within a Gaussian envelope, $e^{-t^2/2}$. The real and imaginary sinusoids, $e^{i2\pi f_0 t}$, differ in phase by a quarter period. The $\pi^{1/4}$ term is a normalization factor which ensures that the wavelet has unit energy. Note that the function given by (A.4) is not really a wavelet as it has a non-zero mean, i.e., the zero frequency term of its corresponding energy spectrum is non-zero and hence it is inadmissible, however, it can be used in practice with $f_0 \gg 0$ with minimal error. The graphical representation of the wavelet transform in time-scale plane is referred to as *scalogram* and it reveals the time evolution of the signal frequency. If the wavelet is complex, then the square modulus represents the energy density distribution of the signal over the time-scale plane.

References

1. Fallen, W.J., Hwang, Y.L., Liguori, J.L., Paulling, J.R., Visineau, G.: Model tests and numerical simulation of ship capsizing in following seas. Final Report, California University Berkeley, Department of Naval Architecture, 226 p. (1980)
2. De Kat, J.O., Paulling, J.R.: Simulation of ship motions and capsizing in severe seas. Trans. - Soc. Nav. Archit. Mar. Eng. **97**, 139–168 (1989)
3. Nayfeh, A.H.: Nonlinear ship dynamics. Technical Report, Virginia Tech, Blacksburg, 17 p., NTIS, Jul (1992)
4. Oh, I.G., Nayfeh, A.H., Mook, D.T.: Theoretical and experimental study of the nonlinearly coupled heave, pitch, and roll motions of a ship in longitudinal waves. In: Proceedings ASME Design Engineering Division on Nonlinear Vibrations, vol. 54, pp. 105–125 (1993)
5. Cotton, B., Spyrou, K.J.: An experimental study of nonlinear behavior in roll and capsize. Int. Shipbuild. Prog. **48**(1), 5–18 (2001)

6. Brown, P.W., Klosinski, W.E.: Damping of a 30 degree deadrise planning boat in roll. Stevens Institute of Technology, Hoboken, NJ. Davidson Laboratory, Final Report for NTIS, 38 p., Jan 1995, NTIS, Springfield, Virginia (1995)
7. Atsavaprance, P., Carneal, J.B., Grant, D., Scott Percival, A.: Experimental investigation of viscous roll damping on the DTMB model 5617 hull form. In: Proceedings of the 26th International Conference on Offshore Mechanics and Arctic Engineering—OMAE, San Diego, CA, vol. 4, pp. 561–570 (2007)
8. Wilson, R.V., Carrica, P.M., Stern, F.: Unsteady RANS method for ship motions with application to roll for a surface combatant. Comput. & Fluids **35**(5), 501–524 (2006)
9. Huang, H., Guo, H.Q., Zhu, R.C., Miao, G.P.: Computations of ship roll damping in viscous flow. Chuan Bo Li Xue/J. Ship Mech. **12**(4), 568–573 (2008) (in Chinese)
10. Bulian, G., Francescutto, A.: Experimental results and numerical simulations on strongly non-linear rolling of multihulls in moderate beam seas. In: Proceedings of the Institution of Mechanical Engineers Part M: Journal of Engineering for the Maritime Environment, vol. 223, pp. 189–210 (2009)
11. Capasso, M., Ferrando, M., Podenzana-Bonvino, C., Cardo, A., Francescutto, A.: Study of the hydrodynamic performances of a trimaran ship for fast transportation. In: Proceedings 1st International Congress on Maritime Transport, Barcelona, pp. 263–273 (2001)
12. Cardo, A., Francescutto, A., Capasso, M., Ferrando, M., Podenzana Bonvino, C.: Hydrodynamic performance in waves of a trimaran ship. In: CD Proceedings of Tenth International Congress of IMAM, Rethimnos, Paper No. 98 (2002)
13. Bulian, G., Francescutto, A., Zotti, I.: Stability and roll motion of fast multihull vessels in beam waves. Ships Offshore Struct. **3**(3), 215–228 (2008)
14. Bhattacharyya, R.: Dynamics of Marine Vehicles. Wiley, New York (1978)
15. Ibrahim, R.A.: Liquid Sloshing Dynamics: Theory and Applications. Cambridge University Press, Cambridge (2005)
16. Senjanović, I., Parunov, J., Ciprić, G.: Safety analysis of ship rolling in rough sea. Chaos Solitons Fractals **8**(4), 659–680 (1997)
17. Liu, L., Tang, Y., Li, H.: Analytical method of capsizing probability in the time domain for ships in the random beam seas. Front. Archit. Civ. Eng. China **1**(3), 361–366 (2007)
18. Schiehlen, W., Seifried, R.: Impact systems with uncertainty. In: Proceedings IUTAM Symposium on Dynamics and Control of Nonlinear Systems, pp. 33–44. Springer, Berlin (2007)
19. Ronsse, R., Sepulchre, R.: Feedback control of impact dynamics: the bouncing ball revisited. In: Proceedings 45th IEEE Conference on Decision and Control, San Diego, CA, pp. 4807–4812 (2006)
20. Addison, P.: The Illustrated Wavelet Transform Handbook. Institute of Physics, Bristol (2002)